



OIST

OKINAWA INSTITUTE OF SCIENCE AND TECHNOLOGY GRADUATE UNIVERSITY
沖縄科学技術大学院大学

Low Reynolds number turbulent flows over elastic walls



Author	Marco E. Rosti, Luca Brandt
journal or publication title	Physics of Fluids
volume	32
number	8
page range	083109
year	2020-08-20
Publisher	AIP Publishing
Rights	(C) 2020 Author(s). This article may be downloaded for personal use only. Any other use requires prior permission of the author and AIP Publishing. This article appeared in Physics of Fluids, 32(8), 083109 (2020) and may be found at https://aip.scitation.org/doi/abs/10.1063/5.0018770 .
Author's flag	publisher
URL	http://id.nii.ac.jp/1394/00001605/

doi: info:doi/10.1063/5.0018770

Low Reynolds number turbulent flows over elastic walls ^{EP}

Cite as: Phys. Fluids **32**, 083109 (2020); <https://doi.org/10.1063/5.0018770>

Submitted: 17 June 2020 . Accepted: 01 August 2020 . Published Online: 20 August 2020

 Marco E. Rosti, and  Luca Brandt

COLLECTIONS

Paper published as part of the special topic on [Fluid-Structure Interactions: From Engineering to Biomimetic SystemsFSI2020](#)

 This paper was selected as an Editor's Pick



View Online



Export Citation



CrossMark

ARTICLES YOU MAY BE INTERESTED IN

[Passive and active control of turbulent flows](#)

Physics of Fluids **32**, 080401 (2020); <https://doi.org/10.1063/5.0022548>

[Transport and fate of human expiratory droplets—A modeling approach](#)

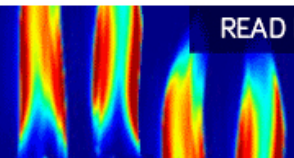
Physics of Fluids **32**, 083307 (2020); <https://doi.org/10.1063/5.0021280>

[Turbulence, pseudo-turbulence, and local flow topology in dispersed bubbly flow](#)

Physics of Fluids **32**, 083310 (2020); <https://doi.org/10.1063/5.0014833>

AIP Advances
Fluids and Plasmas Collection

READ NOW



Low Reynolds number turbulent flows over elastic walls

Cite as: Phys. Fluids 32, 083109 (2020); doi: 10.1063/5.0018770

Submitted: 17 June 2020 • Accepted: 1 August 2020 •

Published Online: 20 August 2020



View Online



Export Citation



CrossMark

Marco E. Rosti^{1,a)}  and Luca Brandt² 

AFFILIATIONS

¹Complex Fluids and Flows Unit, Okinawa Institute of Science and Technology Graduate University, 1919-1 Tancha, Onna-son, Okinawa 904-0495, Japan

²Linné Flow Centre and SeRC (Swedish e-Science Research Centre), KTH Department of Engineering Mechanics, SE 100 44 Stockholm, Sweden

Note: This paper is part of the Special Topic, Fluid-Structure Interactions: From Engineering to Biomimetic Systems.

^{a)}**Author to whom correspondence should be addressed:** marco.rosti@oist.jp

ABSTRACT

We study the laminar and turbulent channel flow over a viscous hyper-elastic wall and show that it is possible to sustain an unsteady chaotic turbulent-like flow at any Reynolds number by properly choosing the wall elastic modulus. We propose a physical explanation for this effect by evaluating the shear stress and the turbulent kinetic energy budget in the fluid and elastic layer. We vary the bulk Reynolds number from 2800 to 10 and identify two distinct mechanisms for turbulence production. At moderate and high Reynolds numbers, turbulent fluctuations activate the wall oscillations, which, in turn, amplify the turbulent Reynolds stresses in the fluid. At a very low Reynolds number, the only production term is due to the energy input from the elastic wall, which increases with the wall elasticity. This mechanism may be exploited to passively enhance mixing in microfluidic devices.

Published under license by AIP Publishing. <https://doi.org/10.1063/5.0018770>

I. INTRODUCTION

In typical microfluidic applications, the Reynolds number is very small, and the flow is laminar. If chaotic mixing is not induced by the device geometry via fully three-dimensional flow fields, mixing is due to molecular diffusion only, resulting in long diffusion times, which limits the efficiency of micro-scale devices. In this context, we study here the feasibility to use a soft elastic wall to enhance mixing by inducing self-sustained chaotic velocity fluctuations also at very low Reynolds numbers.

Several strategies have been proposed in the past to increase mixing in micro-devices, which can be classified into passive and active: in the former, the mixing is enhanced through curved streamlines,^{4,18,24,25,42} while in the latter, the flow is made unsteady by an external actuation.^{2,6,14,15,28} Here, we focus on the possibility to enhance mixing in micro-channels by using elastic walls: the interaction between the soft wall and the flow results in a dynamical instability, which induces transition at very low Reynolds numbers.⁴⁷ In particular, previous linear stability studies^{19,20,39} have

shown that the flow over elastic walls is unstable to infinitesimal disturbances when the Reynolds number exceeds a critical value, which can be tuned by decreasing the shear modulus of the soft wall, thus suggesting that there is an instability even at zero Reynolds number. The existence of this instability has been proved experimentally by Verma and Kumaran,⁴⁶ reaching a transitional Reynolds number of 200 for the softest wall used in the experiments.

Flow instabilities at low Reynolds numbers have been previously observed in the presence of elasticity; in particular, the so-called purely elastic instabilities have been reported for viscoelastic fluids in a wide variety of flow configurations, and they can be generally found when inertial forces are negligible compared to elasticity.^{5,8,23,27,40} Such instabilities are due to the non-linear coupling between the flow and the constitutive equation of the non-Newtonian fluid and lead to the so-called elastic turbulence.^{3,7,13,26,41} Here, we will extend these works by considering a simple Newtonian fluid non-linearly coupled to a viscoelastic wall and show that a self-sustained chaotic flow can be observed.

In this work, we present new Direct Numerical Simulations (DNSs) of the flow over an incompressible hyper-elastic wall at a Reynolds number where turbulence cannot be sustained in channels with rigid walls and show that fluid velocity fluctuations can be sustained by tuning the wall elasticity. In the fluid part of the channel, the full incompressible Navier–Stokes equations are solved, while momentum conservation and incompressibility constraint are enforced inside the solid material. In Sec. II, we first discuss the flow configuration and governing equations and, then, present the numerical methodology used. The effects of a hyper-elastic wall on the channel flow are presented in Sec. III. Finally, a summary of the main findings and some conclusions are drawn in Sec. IV.

II. FORMULATION

We consider the flow of an incompressible viscous fluid through a channel with an incompressible hyper-elastic wall. A sketch of the geometry and the Cartesian coordinate system is reported in Fig. 1: x , y , and z denote the streamwise, wall-normal, and spanwise coordinates, and u , v , and w denote the corresponding velocity components. The channel is bounded by two rigid walls located at $y = 0$ and $2h + h_e$, while the elastic layer extends from $y = 2h$ to $2h + h_e$, where h_e represents the height of the layer, fixed here to $h_e = 0.5h$. In this work, we assume the interface of the elastic layer to be initially flat. Periodic boundary conditions are imposed in the streamwise and spanwise directions.

The fluid and solid phase motion is governed by the conservation of momentum and the incompressibility constraint,

$$\frac{\partial u_i^p}{\partial t} + \frac{\partial u_i^p u_j^p}{\partial x_j} = \frac{1}{\rho} \frac{\partial \sigma_{ij}^p}{\partial x_j} \quad \text{and} \quad \frac{\partial u_i^p}{\partial x_i} = 0, \quad (1)$$

where the suffix p is used to distinguish the fluid^f and solid^s phases. In the previous set of equations, ρ is the density (assumed to be the same for the solid and fluid), and σ_{ij} is the Cauchy stress tensor. The two phases are coupled at the interface by the continuity of the velocity and traction force, i.e., $u_i^f = u_i^s$ and $\sigma_{ij}^f n_j = \sigma_{ij}^s n_j$, where n_i denotes the normal to the interface.

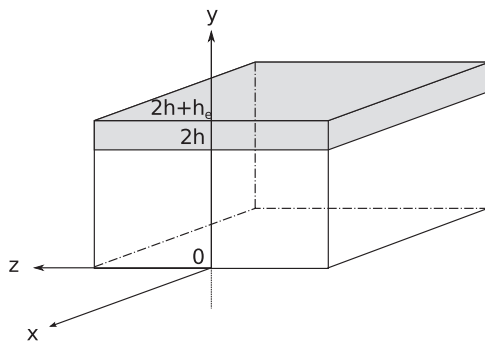


FIG. 1. Sketch of the channel considered in the present work: two solid walls are located at $y = 0$ and $2h + h_e$, while $y = 2h$ indicates the interface between the fluid region and the elastic layer.

To numerically solve the fluid–structure interaction problem at hand, we introduce a monolithic velocity vector field u_i valid everywhere, found by a volume averaging procedure. In particular, we introduce an additional variable ϕ^s , which is the solid volume fraction; this is zero in the fluid and one in the solid, with $0 \leq \phi^s \leq 1$ around the interface. By doing so, we can now write the stress in a mixture form as

$$\sigma_{ij} = (1 - \phi^s) \sigma_{ij}^f + \phi^s \sigma_{ij}^s. \quad (2)$$

This is the so-called one-continuum formulation.⁴⁴ The fluid is Newtonian, and the solid is an incompressible viscous hyper-elastic material with constitutive equations,

$$\sigma_{ij}^f = -p\delta_{ij} + 2\mu\mathcal{D}_{ij} \quad \text{and} \quad \sigma_{ij}^s = -p\delta_{ij} + 2\mu\mathcal{D}_{ij} + G\mathcal{B}_{ij}, \quad (3)$$

where p is the pressure, μ is the dynamic viscosity (assumed to be the same in the two phases), \mathcal{D}_{ij} is the strain rate tensor defined as $\mathcal{D}_{ij} = (\partial u_i / \partial x_j + \partial u_j / \partial x_i) / 2$, and δ_{ij} is the Kronecker delta. The last term in the solid Cauchy stress tensor σ_{ij}^s is the hyper-elastic contribution modeled as a neo-Hookean material, thus satisfying the incompressible Mooney–Rivlin law, where \mathcal{B}_{ij} is the left Cauchy–Green deformation tensor and G is the modulus of transverse elasticity. The full set of equations can be closed in a purely Eulerian manner by updating \mathcal{B}_{ij} and ϕ^s with the following transport equations:

$$\frac{\partial \mathcal{B}_{ij}}{\partial t} + \frac{\partial u_k \mathcal{B}_{ij}}{\partial x_k} = \mathcal{B}_{kj} \frac{\partial u_i}{\partial x_k} + \mathcal{B}_{ik} \frac{\partial u_j}{\partial x_k} \quad \text{and} \quad \frac{\partial \phi^s}{\partial t} + \frac{\partial u_k \phi^s}{\partial x_k} = 0. \quad (4)$$

A. Numerical implementation

The previous set of equations are solved numerically: the time integration is based on an explicit fractional-step method,¹⁶ where all the terms are advanced with the third order Runge–Kutta scheme, except the solid hyper-elastic contribution, which is advanced with the Crank–Nicolson scheme.²⁹ The governing differential equations are solved on a staggered grid using a second order central finite-difference scheme, except for the advection terms in Eq. (4) where the fifth-order WENO scheme is applied. The code has been extensively validated, and more details on the numerical scheme and validation campaign are reported in Refs. 1, 10, 33–35, and 38; more details on the numerical method can be found in the work of Sugiyama *et al.*⁴³

For all the flows considered hereafter, the equations of motion are discretized on a fixed, Cartesian, and uniform mesh with $1296 \times 540 \times 648$ grid points on a computational domain of size $6hk \times 2.5h \times 3hk$ in the streamwise, wall-normal, and spanwise directions. k is a factor used to increase the size of the domain in the homogeneous direction as the Reynolds number decreases;⁴⁵ in particular, $k = 1, 4.30, 18.5, 79.5,$ and 237 for $Re_b = 2800, 651, 151, 35,$ and 11 , respectively. The spatial resolution has been chosen in order to properly resolve the wall deformation for all the Reynolds numbers considered in the present study.³³

III. RESULTS

We study laminar and turbulent channel flows over viscous hyper-elastic walls, together with the baseline cases over stationary

TABLE I. Summary of the DNSs performed, all with a fixed thickness of the elastic layer $h_e = 0.5h$. The table reports the bulk Reynolds number Re_b , the shear elastic modulus G , the mean friction Reynolds number Re_τ , the maximum velocity \bar{u}_M , and its distance from the channel centerline $\hat{y}_M = y_M - h$.

Re_b	$G/(\rho U_b^2)$	\overline{Re}_τ	\bar{u}_M/U_b	\hat{y}_M/h	Re_b	$G/(\rho U_b^2)$	\overline{Re}_τ	\bar{u}_M/U_b	\hat{y}_M/h
2800	∞	180.0	1.16	0.000	151	∞	21.3	1.50	0.000
2800	4.0	180.8	1.17	-0.030	151	1.0	21.8	1.47	-0.069
2800	2.0	203.3	1.19	-0.076	151	0.5	51.0	1.41	-0.222
2800	1.0	240.5	1.23	-0.206	35	∞	10.2	1.50	0.000
2800	0.5	337.0	1.32	-0.386	35	1.0	11.2	1.49	-0.007
651	∞	49.8	1.29	0.000	35	0.5	15.3	1.48	-0.014
651	2.0	49.8	1.30	-0.010	11	∞	5.7	1.50	0.000
651	1.0	68.3	1.33	-0.031	11	0.5	5.7	1.50	0.000
651	0.5	151.1	1.37	-0.463					

impermeable walls. All the simulations are performed at a constant flow rate, and thus, the pressure gradient needed to drive the flow is determined at every time step to ensure this condition; it oscillates around a constant value at a statistical state. The flow Reynolds number is defined based on the bulk velocity, i.e., $Re_b = \rho U_b h / \mu$, where U_b is the average value of the mean velocity computed across the whole domain occupied by the fluid phase; the choice of using U_b and h as the reference velocity and length facilitates the comparison between the flow in a channel with elastic walls and the flow in a channel bounded by rigid walls. In the present work, we vary the bulk Reynolds number Re_b and the modulus of transverse elasticity G . The full set of simulations is reported in Table I. All the simulations start with a fully developed turbulent flow over rigid walls, and then, after an initial transient, a new statistically steady state solution is reached, either laminar or turbulent.

The friction velocity u_τ will be often employed in the following and is defined here as

$$\bar{u}_\tau = \sqrt{\frac{\mu}{\rho} \frac{d\bar{u}}{dy} - \overline{u'v'} + \frac{G}{\rho} \bar{B}_{12}}, \quad (5)$$

where the quantities are evaluated at the mean interface location, $y = 2h$. In the previous relation and in the rest of the work, the overline and the prime represent the mean and fluctuation obtained by averaging over the homogeneous directions and in time. The previous definition is used because, when the channel has moving walls, the friction velocity needs to account for the Reynolds and the elastic shear stresses, which are, in general, non-zero at the solid-fluid interface. Note that the actual value of the friction velocity of the elastic wall is computed from its friction coefficient, found by combining the information of the total C_f , obtained from the driving streamwise pressure gradient, and the one of the lower rigid wall.³³

We start our analysis by studying in Fig. 2 the time evolution of the friction Reynolds number Re_τ , i.e., $u_\tau h / \nu$. In particular, panel (a) shows the friction Reynolds number for the cases with the minimum elastic modulus $G = 0.5\rho U_b^2$, thus corresponding to the most deformable wall, and for different bulk Reynolds numbers Re_b . We observe that, as expected, the friction Reynolds number decreases with the bulk Reynolds number and also the amplitude of its fluctuations. However, different from the flow over rigid walls, the flow

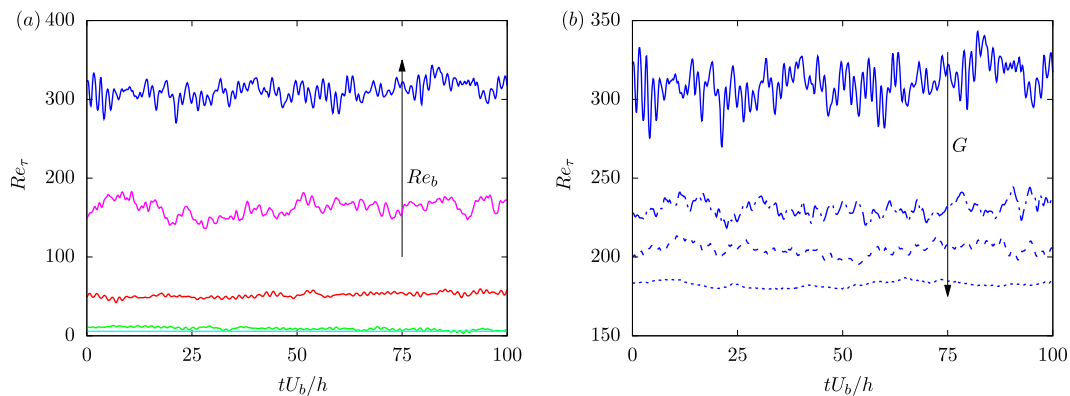


FIG. 2. Time history of the friction Reynolds number Re_τ , space averaged over the wall. The blue, magenta, red, green, and cyan lines are used to distinguish the different bulk Reynolds numbers, $Re_b = 2800, 651, 151, 35, 11$, while the solid, dashed-dotted, dashed, and dotted lines to distinguish the different shear elastic moduli, $G/\rho U_b^2 = 0.5, 1, 2, 4$. In panel (a), the amplitude of the fluctuations is amplified by a factor 5 (magenta line), 10 (red line), and 20 (green line).

remains unstable even for very low Reynolds numbers, $Re_b = 35$ in this case, while a further reduction of the Reynolds number leads to the flow laminarization. If we fix the bulk Reynolds number Re_b and vary only the elastic modulus G , three different behaviors can be observed, as shown by the space and time averaged friction Reynolds number \overline{Re}_τ pertaining all cases studied in the present work collected in Fig. 3(a): (i) for high Re_b , as G increases (the wall becomes more rigid) \overline{Re}_τ decreases eventually saturating at the value obtained for a turbulent flow over rigid walls, see also the time histories in Fig. 2(b); (ii) for intermediate Re_b , as G increases \overline{Re}_τ decreases eventually leading to a fully laminar flow, the friction assuming the same value obtained for a laminar flow over rigid walls; (iii) for low Reynolds numbers, the flow always becomes laminar for any initial condition, and the friction Reynolds number is the same obtained for a laminar flow over rigid walls. Indeed, the thin lines in Fig. 3(a) display the characteristic values for laminar and turbulent channel flows. For every Re_b , reducing the wall elasticity implies a reduction of the resulting \overline{Re}_τ ; all cases converge to the rigid wall solution as G increases, in particular, \overline{Re}_τ converges to the turbulent experimental correlation $0.09(2Re_b)^{0.88}$ (see, e.g., Ref. 32) for $Re_b \gtrsim 482$ and to the laminar analytical solution $\sqrt{3Re_b}$ for $Re_b \lesssim 482$ as $G \rightarrow \infty$.

To quantify the unsteady nature of the flow, we compute the root mean square of the friction velocity $\sqrt{u'_\tau u'_\tau}$, which is used here as a measure of the flow fluctuations. This is divided by its mean value and reported in Fig. 3(b) as a function of the bulk Reynolds number for all the cases considered here. Consistently with the previous discussion, we observe that reducing the wall elasticity induces a reduction in the fluctuations. This reduction is strongly non-linear, with large reduction for increment in small values of G and small reduction for increment in large values of G . In addition, we can observe again that the high Reynolds number cases converge, as G increases, to a non-zero level of fluctuations, i.e., the turbulent rigid wall solution, while the low Reynolds number cases tend to the laminar solution with zero fluctuations. Reducing the Reynolds number,

we observe a further reduction in the fluctuation intensity; also in this case, the variation is strongly non-linear with large reductions in the fluctuation intensity for large Reynolds numbers, while smaller variation is observed at small Re_b , when the flow tends to become laminar. The inset of Fig. 3(b) shows the same quantity, \mathcal{I} , as a function of both Re_b and G as a contour plot obtained by interpolating and extrapolating our data. We observe that, although, in general, \mathcal{I} is a function of both Re_b and G , i.e., $\mathcal{I} = \mathcal{F}(Re_b, G)$, there is a critical value $G^*(Re_b)$ above which the solution does not significantly change anymore with the wall elasticity, and thus, $\mathcal{I} = \mathcal{F}_r(Re_b)$ for $G > G^*$, where \mathcal{F}_r is the solution for the flows over rigid walls. On the other hand, for $G < G^*$, the solution strongly depends on the wall elasticity: this suggests that it is possible to maintain an unsteady chaotic turbulent-like flow, in principle, for any Reynolds number down to 0 as long as the wall shear elastic modulus G is reduced accordingly. If we now replot the data in Fig. 3(b) as a function of a new quantity, obtained as the ratio of the wall elasticity $G/\rho U_b^2$ and the bulk Reynolds number Re_b , we obtain Fig. 4. By doing so, all the non-laminar cases successfully collapse onto a single master curve, decaying with power -0.75 , i.e., $\mathcal{I} \sim (G/\rho U_b^2 Re_b)^{-0.75}$. This behavior further corroborates the idea that the level of fluctuations in the channel can be amplified either by increasing the Reynolds number (at fixed elasticity) or by increasing the wall flexibility, i.e., reducing G (at a fixed Reynolds number).

Next, we characterize the unsteady flows in terms of mean and fluctuation velocities. We start by considering the wall-normal profiles of the mean velocity \bar{u} and turbulent kinetic energy $\mathcal{K} = \rho \overline{u'_i u'_i} / 2$, reported in Figs. 5 and 6. In particular, the left panels of Figs. 5 and 6 show \bar{u} and \mathcal{K} at a fixed Reynolds number ($Re_b = 2800$) and for all the wall elasticities G studied in this work, while the right ones report \bar{u} and \mathcal{K} for a fixed wall elasticity ($G = 0.5\rho U_b^2$) and for all the Reynolds numbers Re_b . From Fig. 5, we observe that the mean velocity of the elastic wall is equal to zero;³³ indeed, the elastic layer can only oscillate around its equilibrium position being attached to

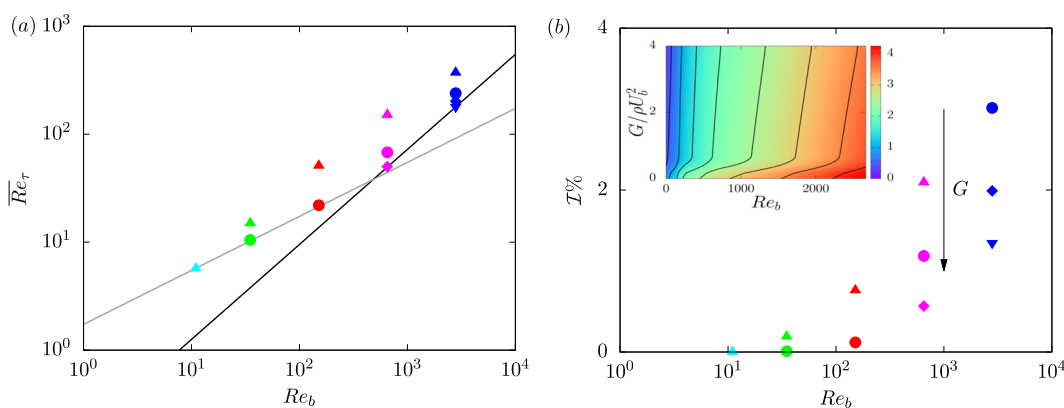


FIG. 3. (a) Mean friction Reynolds number \overline{Re}_τ and (b) root mean square of the friction velocity normalized by its mean, i.e., $\mathcal{I} = \sqrt{u'_\tau u'_\tau} / \bar{u}_\tau$, as a function of the bulk Reynolds number. The blue, magenta, red, green, and cyan colors are used to distinguish different bulk Reynolds numbers $Re_b = 2800, 651, 151, 35,$ and 11 , while the upper-triangle \blacktriangle , circle \bullet , rhombus \blacklozenge , and lower-triangle \blacktriangledown to distinguish different shear elastic moduli $G/\rho U_b^2 = 0.5, 1, 2,$ and 4 . The gray and black lines in panel (a) are the analytical solutions for laminar flows and the experimental correlation for turbulent flows, respectively. The inset in panel (b) reports the contour of $\mathcal{I}\%$ as a function of the Reynolds number Re_b and elastic shear modulus G obtained by interpolation and extrapolation of our data. The black lines are separated by 0.5 .

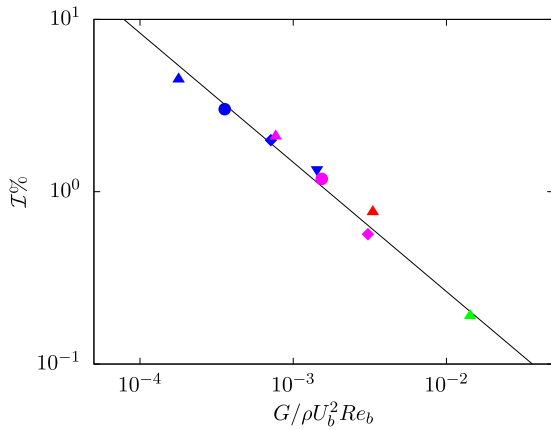


FIG. 4. Root mean square of the friction velocity normalized by its mean, i.e., $\mathcal{I} = \sqrt{\overline{u_i' u_i'}} / \bar{u}_\tau$, as a function of the ratio of the normalized wall elasticity G and bulk Reynolds number, i.e., $G/\rho U_b^2 Re_b$. The blue, magenta, red, and green colors are used to distinguish different bulk Reynolds numbers $Re_b = 2800, 651, 151,$ and 35 , while the upper-triangle \blacktriangle , circle \bullet , rhombus \blacklozenge , and lower-triangle \blacktriangledown are used to distinguish different shear elastic moduli $G/\rho U_b^2 = 0.5, 1, 2,$ and 4 .

the top stationary rigid wall. Although the mean velocity is zero inside this layer, the elastic layer induces profound modification of the fluid flow in the channel. In particular, the mean velocity profile becomes more skewed, with its maximum \bar{u}_M increasing and located closer to the rigid wall as the elasticity increases (G decreases), as shown in Fig. 5(a). Note that an inflection point in the mean profile appears within the fluid region ($0 < y < 2h$), usually associated with the occurrence of a Kelvin–Helmholtz instability and the formation of large scale spanwise-correlated rollers.^{12,21,22,30,31,33,36,37} When the Reynolds number is decreased (right panel), the asymmetry in the flow reduces with the maximum velocity increasing and its location moving back toward the channel center.

Eventually, the laminar analytical profile is recovered for the smallest Re_b considered.

When focusing on the velocity fluctuations in Fig. 6(a), we observe that the turbulent kinetic energy \mathcal{K} is higher close to the elastic wall than close to the rigid wall, with the maximum value becoming almost the double of the peak close to the bottom wall for the most deformable case (left panel). This is due to the movement of the deformable wall, which strongly increases the velocity fluctuations, especially the ones in the wall-normal directions, i.e., v' (see, e.g., Ref. 33). Furthermore, the near-wall peaks of the turbulent kinetic energy move farther from the elastic walls as the elasticity is increased. The turbulent fluctuations have non-zero values at $y = 2h$ for the elastic cases since the no-slip condition is now enforced on a wall, which is moving, i.e., $u_i^f = u_i^s$. In particular, \mathcal{K} does not clearly vanish until reaching the rigid top wall ($y = 2.5h$), thus indicating that the fluctuations propagate deeply inside the solid layer. The asymmetry in the flow originates from the asymmetry of the geometry; this induces the shift of the minimum of \mathcal{K} toward the rigid walls, as well as the shift in the same direction of the maximum velocity, as reported in Table I.

Figure 6(b) shows how the turbulent kinetic energy \mathcal{K} scales with the Reynolds number, for a fixed wall elasticity; in particular, the softest wall is considered here. We observe that as Re_b decreases, the peak of turbulent kinetic energy close to the rigid wall rapidly vanishes, as expected for flows over rigid walls, where the lowest Reynolds number able to sustain a turbulent flow is around 600, as reported by Tsukahara *et al.*⁴⁵ A similar trend is evident for the peak close to the moving wall, but the decrease is much lower than for a rigid wall. Indeed, for $Re_b < 600$, the near-wall peak close to the rigid wall completely disappears, and the profiles exhibit a single peak close to the elastic wall. In addition, the peak moves away from the deformable wall toward the bulk of the channel as the Reynolds number reduces, indicating that all the turbulent fluctuations in the channel at low Re_b are produced by the moving wall, then propagating across the channel.

Apart from the diagonal components of the Reynolds stress tensor discussed above in terms of the turbulent kinetic energy,

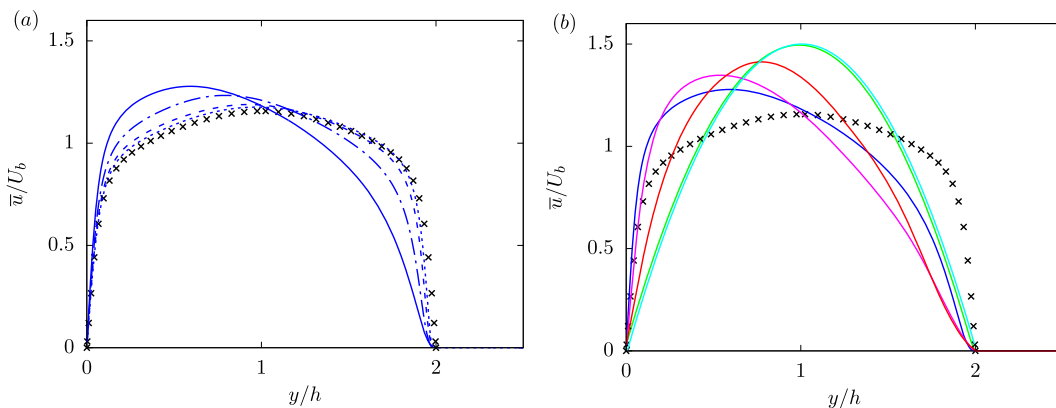


FIG. 5. Mean velocity profile \bar{u} as a function of the wall-normal distance y for (a) different wall elastic moduli G at $Re_b = 2800$ and for (b) different Reynolds numbers Re_b with $G = 0.5\rho U_b^2$. The line colors and styles are the same, as in Fig. 2. The symbols represent the profiles from the DNS by Kim, Moin, and Moser¹⁷ of turbulent flow between two solid rigid walls plotted as a reference.

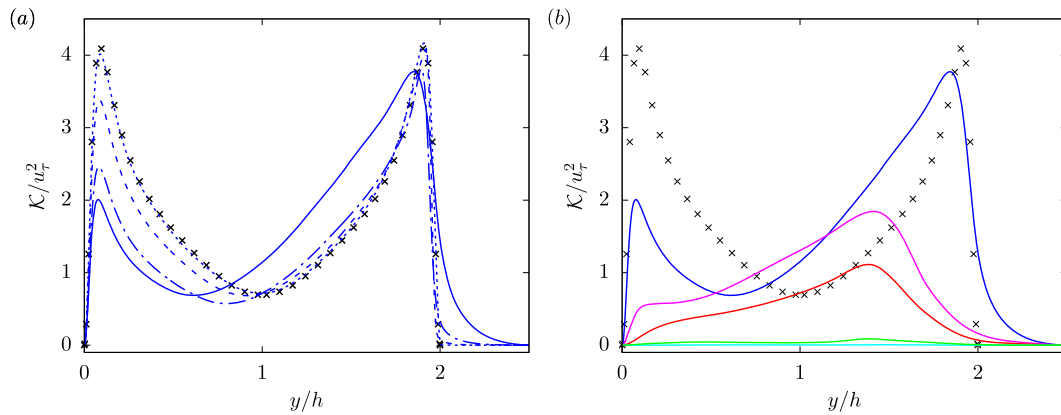


FIG. 6. Mean turbulent kinetic energy \mathcal{K} as a function of the wall-normal distance y for (a) different wall elastic moduli G at $Re_b = 2800$ and for (b) different Reynolds numbers Re_b with $G = 0.5\rho U_b^2$. The line colors and styles are the same, as in Fig. 2. The symbols represent the profiles from the DNS by Kim, Moin, and Moser¹⁷ of turbulent flow between two solid rigid walls plotted as a reference.

another important observable is the off-diagonal shear component of the Reynolds stress tensor $-\rho\overline{u'v'}$, which together with the mean viscous $\mu d\overline{u}/dy$ and elastic stress $G\overline{B}_{12}$ shear components form the total shear stress, i.e.,

$$\tau = \mu d\overline{u}/dy - \rho\overline{u'v'} + G\overline{B}_{12}. \quad (6)$$

All these are reported in Fig. 7(a) for the cases at $Re_b = 2800$ (solid lines). The cross Reynolds stress component is strongly affected by the presence of the moving wall: the maximum value increases and moves away from the wall as the elasticity increases at a fixed Reynolds number. The stress profiles vary linearly in the bulk of the channel away from the wall, although with different slopes

depending on Re_b and G . Most of these effects are well compensated in Fig. 7 by dividing \tilde{y} with $\tilde{y}_M = 2h - y_M$, i.e., the distance of the location of the maximum mean velocity from the elastic wall. At the interface, the value of the stress is not null as in the rigid case; however, inside the elastic layer, the Reynolds shear stress vanishes quickly. The mean viscous stress is almost null in the solid and the bulk of the channel and exhibits a small peak close to the interface, which increases as G increases, i.e., the wall is more rigid, eventually having the maximum at the interface for the completely rigid case; the elastic stress, on the contrary, is null in the fluid region and almost the total stress in the solid layer. Thus, we can conclude that the total shear stress is dominated by the elastic stress in the solid layer, by the Reynolds stress in the bulk of the

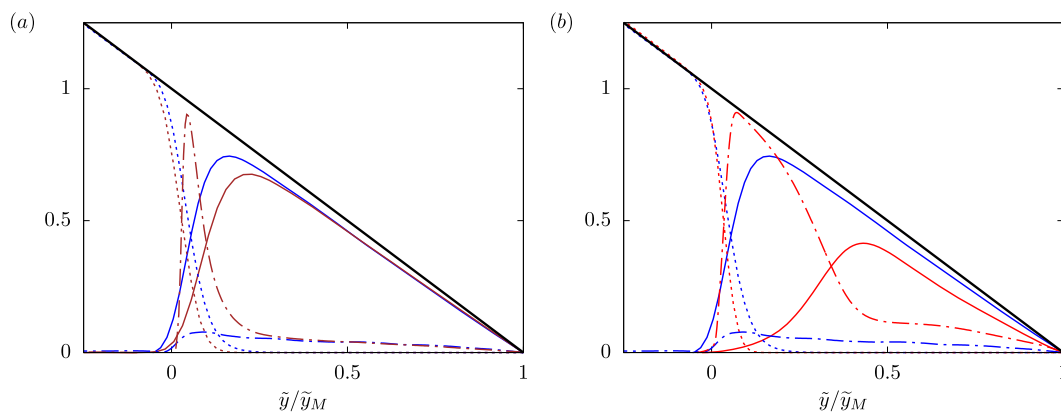


FIG. 7. Reynolds shear stress $-\rho\overline{u'v'}$ (solid line), viscous stress $\mu d\overline{u}/dy$ (dashed-dotted line), and shear elastic stress $G\overline{B}_{12}$ (dotted line) in wall units as a function of the wall-normal distance from the elastic wall $\tilde{y} = 2h - y$ normalized by $\tilde{y}_M = 2h - y_M$ for (a) different wall elastic moduli G at $Re_b = 2800$ and for (b) different Reynolds numbers Re_b with $G = 0.5\rho U_b^2$. The values of y_M used to normalize the different abscissa can be obtained from Table I. In particular, the blue, brown, and red colors in the two panels are used for the cases $Re_b = 2800$ and $G = 0.5\rho U_b^2$, $Re_b = 2800$ and $G = 4\rho U_b^2$, and $Re_b = 151$ and $G = 0.5\rho U_b^2$.

channel and the balance of all the three components at the interface, with the relative contributions at the interface strongly changing with G : for rigid walls, the dominant and only contribution not null at the interface is the viscous stress, while for flexible walls, the Reynolds and elastic stresses grow with the wall elasticity. When the Reynolds number is varied, the balance between the three terms is significantly altered, as shown in Fig. 7(b). Indeed, as the Reynolds numbers decrease, the Reynolds shear stress peak shifts away from the wall, thus reducing its total contribution. On the other hand, the viscous contribution increases and compensates for the loss of Reynolds shear stress. For the lowest Reynolds number (not shown in Fig. 7), the flow is fully laminar, and the total stress is equal to the elastic stress in the solid layer and the viscous stress in the fluid region, with the Reynolds shear stress being null. From Fig. 7, we can conclude that, different from the flow over rigid walls, the turbulent fluctuations do not rapidly vanish when reducing the Reynolds number because of their persistence in the bulk of the channel.

To confirm these observations, we consider the turbulent kinetic energy balance. To do so, we decompose the velocity field $u_i(x, y, z, t)$ into its mean $\bar{u}_i(y)$ and fluctuation $u'_i(x, y, z, t)$ as $u_i = \bar{u}_i + u'_i$. By substituting this into the governing equation, we obtain

$$\rho \left(\frac{\partial u'_i}{\partial t} + \frac{\partial u'_i u'_j}{\partial x_j} + \frac{\partial \bar{u}_i u'_j}{\partial x_j} + \frac{\partial u'_i \bar{u}_j}{\partial x_j} + \frac{\partial \bar{u}_i \bar{u}_j}{\partial x_j} \right) = -\frac{\partial p}{\partial x_i} + 2\mu \frac{\partial \mathcal{D}_{ij}}{\partial x_j} + G \frac{\partial \phi^s \mathcal{B}_{ij}}{\partial x_j}, \quad (7)$$

which can be rewritten for later convenience as

$$\rho \left(\frac{\partial u'_i}{\partial t} + \frac{\partial u'_i u'_j}{\partial x_j} + u'_i \frac{\partial \bar{u}_i}{\partial x_j} + \frac{\partial u'_i \bar{u}_j}{\partial x_j} + \frac{\partial \bar{u}_i \bar{u}_j}{\partial x_j} \right) = -\frac{\partial p}{\partial x_i} + 2\mu \frac{\partial \mathcal{D}_{ij}}{\partial x_j} + G \frac{\partial \phi^s \mathcal{B}_{ij}}{\partial x_j}. \quad (8)$$

We now multiply the equation by u'_i and obtain

$$\rho \left(\frac{\partial u'_i u'_i / 2}{\partial t} + \frac{\partial u'_i u'_i u'_j / 2}{\partial x_j} + u'_i u'_j \frac{\partial \bar{u}_i}{\partial x_j} + \frac{\partial u'_i u'_i \bar{u}_j / 2}{\partial x_j} + u'_i \frac{\partial \bar{u}_i \bar{u}_j}{\partial x_j} \right) = -\frac{\partial u'_i p}{\partial x_i} + 2\mu \frac{\partial u'_i \mathcal{D}_{ij}}{\partial x_j} - 2\mu \mathcal{D}_{ij} \mathcal{D}'_{ij} + G \frac{\partial u'_i \phi^s \mathcal{B}_{ij}}{\partial x_j} - G \phi^s \mathcal{B}_{ij} \mathcal{D}'_{ij}, \quad (9)$$

where we made use of

$$u'_i \frac{\partial \mathcal{D}_{ij}}{\partial x_j} = \frac{\partial u'_i \mathcal{D}_{ij}}{\partial x_j} - \mathcal{D}'_{ij} \frac{\partial u'_i}{\partial x_j} = \frac{\partial u'_i \mathcal{D}_{ij}}{\partial x_j} - \mathcal{D}'_{ij} \mathcal{D}'_{ij} \quad (10)$$

and, similarly, of

$$u'_i \frac{\partial \phi^s \mathcal{B}_{ij}}{\partial x_j} = \frac{\partial u'_i \phi^s \mathcal{B}_{ij}}{\partial x_j} - \phi^s \mathcal{B}'_{ij} \frac{\partial u'_i}{\partial x_j} = \frac{\partial u'_i \phi^s \mathcal{B}_{ij}}{\partial x_j} - \phi^s \mathcal{B}_{ij} \mathcal{D}'_{ij}, \quad (11)$$

where the last substitution is possible being \mathcal{D}_{ij} and \mathcal{B}_{ij} symmetric tensors. The equation above can then be volume averaged with the operator

$$\langle \cdot \rangle = \frac{1}{V} \int_V \cdot dV, \quad (12)$$

leading to the equation

$$\rho \left(\frac{\partial \langle u'_i u'_i \rangle / 2}{\partial t} + \langle u'_i u'_i \rangle \frac{\partial \bar{u}_i}{\partial x_j} \right) = -2\mu \langle \mathcal{D}'_{ij} \mathcal{D}'_{ij} \rangle - G \langle \phi^s \mathcal{B}_{ij} \mathcal{D}'_{ij} \rangle. \quad (13)$$

Here, all the transport terms $\langle \partial u'_i \mathcal{F}_{ij} / \partial x_j \rangle$ vanish due to the homogeneity of the domain and the no-slip and no-penetration boundary conditions at the rigid walls, and the terms $\langle u'_i \partial \bar{u}_i \bar{u}_j / \partial x_j \rangle$ and $\langle \bar{\mathcal{D}}_{ij} \mathcal{D}'_{ij} \rangle$ vanish because $\langle u'_i \rangle = 0$ and $\langle \mathcal{D}'_{ij} \rangle = 0$ due to ergodicity. Finally, we obtain the turbulent kinetic energy equation,

$$\frac{d\mathcal{K}}{dt} = \mathcal{P} - \varepsilon - \psi_G, \quad (14)$$

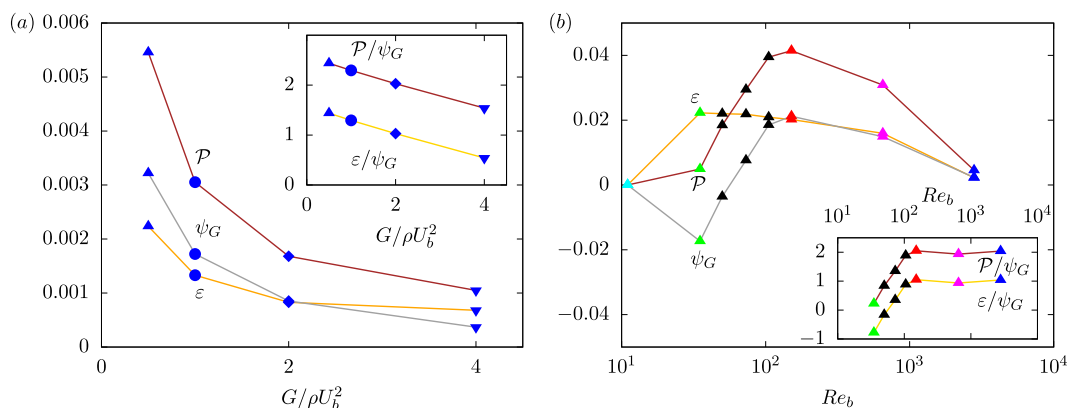


FIG. 8. Volume averaged turbulent production \mathcal{P} (brown), turbulent dissipation ε (orange), and power of the elastic wall ψ_G (gray) as a function of the wall elasticity G for a fixed Reynolds number $Re_b = 2800$ (a) and as a function of the Reynolds number Re_b for a fixed wall elasticity $G = 0.5\rho U_b^2$ (b). The symbol style is the same, as in Fig. 3, with the addition of the black triangles, additional simulations included for the sake of clarity. The two insets show the production \mathcal{P} and dissipation ε rates divided by the power of the elastic wall ψ_G .

where the different terms indicate the rate of change of turbulent kinetic energy \mathcal{K} , the turbulent production rate \mathcal{P} , the dissipation rate ε , and the power of the elastic wall ψ_G , defined as

$$\begin{aligned}\mathcal{K} &= \rho \langle u'_i u'_i \rangle / 2, \quad \mathcal{P} = -\rho \langle u'_1 u'_2 \frac{\partial \bar{u}_1}{\partial x_2} \rangle, \\ \varepsilon &= 2 \mu \langle \mathcal{D}'_{ij} \mathcal{D}'_{ij} \rangle, \quad \psi_G = G \langle \phi^s \mathcal{B}_{ij} \mathcal{D}'_{ij} \rangle.\end{aligned}\quad (15)$$

ψ_G is the rate of work performed by the fluid on the elastic wall that can be either positive or negative and, thus, a sink or source of turbulent kinetic energy. At a statistically steady state, the time derivative is obviously null, and thus, Eq. (14) reduces to a balance between \mathcal{P} , ε , and ψ_G .

These three terms are displayed in Fig. 8 as a function of the shear elastic modulus G (left panel) and the Reynolds number Re_b (right panel). In the left panel, we see that the elastic power contribution is positive, and indeed, the presence of the elastic wall acts as an additional dissipation term at a high Reynolds number. This term reduces as G increases, eventually vanishing for perfectly rigid walls when $G \rightarrow \infty$. On the other hand, the behavior at fixed G is non-monotonic with Re_b : as Re_b decreases, all the terms first increase, reach a maximum, and then decrease. In particular, all the terms grow by a factor of around 10 when decreasing the Reynolds number from 2800 to 151. Interestingly, while the turbulent production rapidly vanishes as the flow is approaching the laminar flow (for $Re_b \lesssim 151$), the power of the elastic walls changes the sign and becomes a production term for the turbulent kinetic energy. Because of this, the flow can remain turbulent at much lower Reynolds numbers than what usually found for flows over rigid walls, and by choosing properly the value of G , fluctuations can be sustained at any small Reynolds number. In conclusion, while at a high Reynolds number, the standard wall cycle¹¹ takes place (although slightly modified by the elastic walls³³), at a low Reynolds number, a different mechanism arises to sustain the chaotic flow: this new mechanism originates from the non-linear interaction between the elastic solid and the fluid and resembles what found at low Reynolds and high Weissenberg numbers (i.e., high elasticity numbers) for non-Newtonian fluids.⁷⁻⁹

IV. CONCLUSIONS

We have carried out a number of direct numerical simulations of laminar and turbulent channel flows over a viscous hyper-elastic wall. The flow inside the fluid region is described by the Navier-Stokes equations, while momentum conservation and incompressibility are imposed inside the solid layer. The two sets of equations are coupled using a one-continuum formulation allowing a fully Eulerian description of the multiphase flow problem. Here, we systematically reduce the Reynolds number and vary the wall elasticity to identify in which condition a chaotic unsteady flow can be sustained.

In general, the friction Reynolds number Re_τ is a function of both the bulk Reynolds number Re_b and the wall shear elastic modulus G : we show that reducing the wall elasticity leads to a reduction in the resulting friction Reynolds number, with the value converging to the value of the turbulent flow over rigid walls for $Re_b \gtrsim 482$ and to the laminar analytical solution for $Re_b \lesssim 482$. There is, therefore,

a critical value G^* above which the solution does not change anymore with the wall elasticity and the flow behaves as in the presence of rigid walls. More interestingly, for $G < G^*$, the solution depends on the wall elasticity: the mean friction and the velocity fluctuations increase with the wall deformability, and it is possible to maintain an unsteady chaotic turbulent-like flow, in principle, for any Reynolds number, i.e., in conditions where a standard flow over rigid walls would be laminar, as long as the wall shear elastic modulus G is properly reduced.

We show that at a low Reynolds number, the velocity fluctuations are mainly generated by the elastic wall, while the fluctuations close to the rigid wall rapidly vanish. As we reduce Re_b to values of order 100, we observe an increase in the velocity fluctuations due to strong wall oscillations, associated with an increase in the turbulent production \mathcal{P} . The power of the elastic wall is a dissipation term, approximately of the same order of the viscous dissipation, thus promoting the fragmentation of typical coherent structures and the consequent formation of small scale structures. Further reducing the bulk Reynolds number, \mathcal{P} decreases as the Reynolds stresses decrease in the shear layer close to the elastic wall and remain strong only in the bulk of the channel where the mean shear is negligible. On the other hand, the power of the elastic wall changes the sign and becomes a source of turbulence kinetic energy, mostly balanced by the viscous dissipation. At a fixed shear elastic modulus, the flow eventually laminarizes, which can be compensated by a reduction of G , which monotonically increases the fluctuations in the flow. Indeed, we found that the level of fluctuations scale approximately as $\sim (G/Re_b)^{-0.75}$. Thus, we can conclude that the chaotic flow at very low Reynolds numbers is mainly sustained by the elastic wall oscillations, which produce turbulent kinetic energy at the interface, and then transferred to the fluid through viscous stresses; this process sustains non-zero Reynolds stresses in the bulk of the channel.

The present results can have profound influence on the development of strategies to increase mixing in microfluidic devices by exploiting a dynamical instability associated with the coupling between the flow and an elastic wall.

ACKNOWLEDGMENTS

The authors acknowledge computer time provided by the Swedish National Infrastructure for Computing (SNIC) and the Scientific Computing Section of Research Support Division at OIST. L.B. acknowledges financial support from the Swedish Research Council, VR Grant No. 2016-06119, hybrid multiscale modeling of transport phenomena for energy efficient processes.

DATA AVAILABILITY

The data that support the findings of this study are available from the corresponding author upon reasonable request.

REFERENCES

- ¹D. Aghalibi, M. E. Rosti, and L. Brandt, "Inertial migration of a deformable particle in pipe flow," *Phys. Rev. Fluids* **4**(10), 104201 (2019).
- ²M. Z. Bazant and T. M. Squires, "Induced-charge electrokinetic phenomena: Theory and microfluidic applications," *Phys. Rev. Lett.* **92**(6), 066101 (2004).

- ³S. Berti and G. Boffetta, “Elastic waves and transition to elastic turbulence in a two-dimensional viscoelastic Kolmogorov flow,” *Phys. Rev. E* **82**(3), 036314 (2010).
- ⁴F. G. Bessoth, A. J. Manz *et al.*, “Microstructure for efficient continuous flow mixing,” *Anal. Commun.* **36**(6), 213–215 (1999).
- ⁵K. Gardner, E. R. Pike, M. J. Miles, A. Keller, and K. Tanaka, “Photon-correlation velocimetry of polystyrene solutions in extensional flow fields,” *Polymer* **23**(10), 1435–1442 (1982).
- ⁶I. Glasgow and N. Aubry, “Enhancement of microfluidic mixing using time pulsing,” *Lab Chip* **3**(2), 114–120 (2003).
- ⁷A. Groisman and V. Steinberg, “Elastic turbulence in a polymer solution flow,” *Nature* **405**(6782), 53–55 (2000).
- ⁸S. J. Haward, G. H. McKinley, and A. Q. Shen, “Elastic instabilities in planar elongational flow of monodisperse polymer solutions,” *Sci. Rep.* **6**, 33029 (2016).
- ⁹C. C. Hopkins, S. J. Haward, and A. Q. Shen, “Purely elastic fluid-structure interactions in microfluidics: Implications for mucociliary flows,” *Small* **16**(9), 1903872 (2020).
- ¹⁰D. Izbassarov, M. E. Rosti, M. N. Ardekani, M. Sarabian, S. Hormozi, L. Brandt, and O. Tammisola, “Computational modeling of multiphase viscoelastic and elastoviscoplastic flows,” *Int. J. Numer. Methods Fluids* **88**(12), 521–543 (2018).
- ¹¹J. Jiménez and A. Pinelli, “The autonomous cycle of near-wall turbulence,” *J. Fluid Mech.* **389**, 335359 (1999).
- ¹²J. Jiménez, M. Uhlmann, A. Pinelli, and G. Kawahara, “Turbulent shear flow over active and passive porous surfaces,” *J. Fluid Mech.* **442**, 89–117 (2001).
- ¹³D. Kawale, E. Marques, P. L. J. Zitha, M. T. Kreutzer, W. R. Rossen, and P. E. Boukany, “Elastic instabilities during the flow of hydrolyzed polyacrylamide solution in porous media: Effect of pore-shape and salt,” *Soft Matter* **13**(4), 765–775 (2017).
- ¹⁴S. Kazemi, V. Nourian, M. R. H. Nobari, and S. Movahed, “Two dimensional numerical study on mixing enhancement in micro-channel due to induced charge electrophoresis,” *Chem. Eng. Process.* **120**, 241–250 (2017).
- ¹⁵B. Keshavarzian, M. Shamschiri, M. Charmiyan, and A. Moaveni, “Optimization of an active electrokinetic micromixer based on the number and arrangement of microelectrodes,” *J. Appl. Fluid Mech.* **11**(6), 1531–1541 (2018).
- ¹⁶J. Kim and P. Moin, “Application of a fractional-step method to incompressible Navier–Stokes equations,” *J. Comput. Phys.* **59**(2), 308–323 (1985).
- ¹⁷J. Kim, P. Moin, and R. Moser, “Turbulence statistics in fully developed channel flow at low Reynolds number,” *J. Fluid Mech.* **177**, 133–166 (1987).
- ¹⁸J. B. Knight, A. Vishwanath, J. P. Brody, and R. H. Austin, “Hydrodynamic focusing on a silicon chip: Mixing nanoliters in microseconds,” *Phys. Rev. Lett.* **80**(17), 3863 (1998).
- ¹⁹V. Kumaran, “Stability of inviscid flow in a flexible tube,” *J. Fluid Mech.* **320**, 1–17 (1996).
- ²⁰V. Kumaran and R. Muralikrishnan, “Spontaneous growth of fluctuations in the viscous flow of a fluid past a soft interface,” *Phys. Rev. Lett.* **84**(15), 3310 (2000).
- ²¹Y. Kuwata and K. Suga, “Transport mechanism of interface turbulence over porous and rough walls,” *Flow, Turbul. Combust.* **97**(4), 1071–1093 (2016).
- ²²Y. Kuwata and K. Suga, “Extensive investigation of the influence of wall permeability on turbulence,” *Int. J. Heat Fluid Flow* **80**, 108465 (2019).
- ²³R. G. Larson, “Instabilities in viscoelastic flows,” *Rheol. Acta* **31**(3), 213–263 (1992).
- ²⁴C.-Y. Lee, C.-L. Chang, Y.-N. Wang, and L.-M. Fu, “Microfluidic mixing: A review,” *Int. J. Mol. Sci.* **12**(5), 3263–3287 (2011).
- ²⁵C.-Y. Lee, W.-T. Wang, C.-C. Liu, and L.-M. Fu, “Passive mixers in microfluidic systems: A review,” *Chem. Eng. J.* **288**, 146–160 (2016).
- ²⁶E. J. Lim, T. J. Ober, J. F. Edd, S. P. Desai, D. Neal, K. W. Bong, P. S. Doyle, G. H. McKinley, and M. Toner, “Inertio-elastic focusing of bioparticles in microchannels at high throughput,” *Nat. Commun.* **5**(1), 1–9 (2014).
- ²⁷G. H. McKinley, P. Pakdel, and A. Öztekin, “Rheological and geometric scaling of purely elastic flow instabilities,” *J. Non-Newtonian Fluid Mech.* **67**, 19–47 (1996).
- ²⁸G. A. Mensing, T. M. Pearce, M. D. Graham, and D. J. Beebe, “An externally driven magnetic microstirrer,” *Philos. Trans. R. Soc., A* **362**(1818), 1059–1068 (2004).
- ²⁹T. Min, J. Y. Yoo, and H. Choi, “Effect of spatial discretization schemes on numerical solutions of viscoelastic fluid flows,” *J. Non-Newtonian Fluid Mech.* **100**(1), 27–47 (2001).
- ³⁰A. Monti, M. Omidyeganeh, B. Eckhardt, and A. Pinelli, “On the genesis of different regimes in canopy flows—A numerical investigation,” *J. Fluid Mech.* **891**, A9 (2020).
- ³¹A. Monti, M. Omidyeganeh, and A. Pinelli, “Large-eddy simulation of an open-channel flow bounded by a semi-dense rigid filamentous canopy: Scaling and flow structure,” *Phys. Fluids* **31**(6), 065108 (2019).
- ³²S. B. Pope, *Turbulent Flows* (Cambridge University Press, 2001).
- ³³M. E. Rosti and L. Brandt, “Numerical simulation of turbulent channel flow over a viscous hyper-elastic wall,” *J. Fluid Mech.* **830**, 708–735 (2017).
- ³⁴M. E. Rosti and L. Brandt, “Suspensions of deformable particles in a Couette flow,” *J. Non-Newtonian Fluid Mech.* **262**(C), 3–11 (2018).
- ³⁵M. E. Rosti, L. Brandt, and D. Mitra, “Rheology of suspensions of viscoelastic spheres: Deformability as an effective volume fraction,” *Phys. Rev. Fluids* **3**(1), 012301(R).
- ³⁶M. E. Rosti, L. Brandt, and A. Pinelli, “Turbulent channel flow over an anisotropic porous wall - drag increase and reduction,” *J. Fluid Mech.* **842**, 381–394 (2018).
- ³⁷M. E. Rosti, L. Cortezzi, and M. Quadrio, “Direct numerical simulation of turbulent channel flow over porous walls,” *J. Fluid Mech.* **784**, 396–442 (2015).
- ³⁸M. E. Rosti, S. Pramanik, L. Brandt, and D. Mitra, “The breakdown of Darcy’s law in a soft porous material,” *Soft Matter* **16**, 939 (2020).
- ³⁹V. Shankar and V. Kumaran, “Stability of non-parabolic flow in a flexible tube,” *J. Fluid Mech.* **395**, 211–236 (1999).
- ⁴⁰E. S. G. Shaqfeh, “Purely elastic instabilities in viscometric flows,” *Annu. Rev. Fluid Mech.* **28**(1), 129–185 (1996).
- ⁴¹V. Steinberg, “Scaling relations in elastic turbulence,” *Phys. Rev. Lett.* **123**(23), 234501 (2019).
- ⁴²A. D. Stroock, S. K. W. Dertinger, A. Ajdari, I. Mezic, H. A. Stone, and G. M. Whitesides, “Chaotic mixer for microchannels,” *Science* **295**(5555), 647–651 (2002).
- ⁴³K. Sugiyama, S. Ii, S. Takeuchi, S. Takagi, and Y. Matsumoto, “A full Eulerian finite difference approach for solving fluid-structure coupling problems,” *J. Comput. Phys.* **230**(3), 596–627 (2011).
- ⁴⁴G. Tryggvason, M. Sussman, and M. Y. Hussaini, “Immersed boundary methods for fluid interfaces,” *Comput. Methods Multiphase Flow* **3**, 37–77 (2007).
- ⁴⁵T. Tsukahara, Y. Seki, H. Kawamura, and D. Tochio, “DNS of turbulent channel flow at very low Reynolds numbers,” in *TSFP Digital Library Online* (Begel House, Inc., 2005).
- ⁴⁶M. K. S. Verma and V. Kumaran, “A dynamical instability due to fluid-wall coupling lowers the transition Reynolds number in the flow through a flexible tube,” *J. Fluid Mech.* **705**, 322–347 (2012).
- ⁴⁷M. K. S. Verma and V. Kumaran, “A multifold reduction in the transition Reynolds number, and ultra-fast mixing, in a micro-channel due to a dynamical instability induced by a soft wall,” *J. Fluid Mech.* **727**, 407–455 (2013).